atoms

MDPI

Article

Instrument Development for Lunar Interior Investigation Using Atom Interferometry

Yun-Jhih Chen *, Filippo Borselli †, Sheng-wey Chiow and Nan Yu

Jet Propulsion Laboratory, California Institute of Technology, Pasadena, CA 91109, USA
* Correspondence: yun-jhih.chen@jpl.nasa.gov
† Current address: Welinq, 75005 Paris, France.

Abstract

The Atomic Lunar Seismometer (ALS) is an atom-interferometer instrument concept for measuring the lunar gravity and vibration modes at long time scales. Compared to other seismometer techniques, atom interferometers offer a pathway toward an ultra-low drift seismometer for signals around and below the mHz frequency range. The ALS instrument concept is also applicable to other terrestrial bodies such as Mars. In this paper, we present our instrument design based on a 5 cm tall atomic fountain and summarize the test results obtained in a laboratory environment. This development is specifically to optimize and accommodate in lunar environment. Presently, the instrument's short-term sensitivity is 1.4×10^{-6} m/s^2/$\sqrt{\text{Hz}}$ (140 μGal/$\sqrt{\text{Hz}}$), limited by the vibration noise in our lab, and it averages down to 6.7×10^{-8} m/s^2 (6.7 μGal) after 445 s.

Keywords: atom interferometry; gravimeter; lunar seismometer

1. Introduction

Understanding the origin and evolution of planetary bodies is a primary objective of planetary science and is crucial for the expansion of humanity beyond Earth. Insight into a planet's interior is essential for reconstructing its geological history. Gravimetry and seismology are among the foremost methods for probing planetary interiors [1] including Earth [2,3]. Despite limited seismic stations, Apollo-era seismic data continue to shape our understanding of the lunar interior [4,5]. Measurements of the lunar gravitational field with orbiters such as GRAIL [6–8] have further advanced our knowledge. Nonetheless, a long-lived seismic network on the lunar surface is still highly desired. The Apollo instruments were not sensitive enough in the mHz frequency range to observe the fundamental vibration mode of the Moon. Newer mission concepts, such as the Lunar Geophysical Network [9] or the Farside Seismic Suite [10], will deploy improved seismometers on the Moon.

The Atomic Lunar Seismometer (ALS) aims to improve seismometer technology by combining seismic wave sensing and absolute gravitational field measurement into a single instrument. ALS uses laser-cooled atoms as free-falling test masses and their matter-wave properties to sense seismic waves and the local gravitational field. Under constant gravity, time-varying signals reflect ground seismic motion, while a stationary ground surface yields a signal representing the local gravity.

ALS is based on the atom-interferometric technique, and its application will focus on signals in the mHz frequency range, where alternative seismometer techniques tend to exhibit large drift [11,12]. The low-frequency range is essential for studying the fundamental

Check for updates

Academic Editor: Mark Edwards

Received: 16 May 2026
Revised: 12 August 2026
Accepted: 14 August 2026
Published: 15 September 2026

Copyright: © 2026 by the authors. Licensee MDPI, Basel, Switzerland. This article is an open access article distributed under the terms and conditions of the Creative Commons Attribution (CC BY) license.

vibration modes of a planetary body and its response to gravitational waves [13]. Atom interferometers may deliver ultra-low-drift measurement because its working principle traces back to intrinsic properties of atoms; however, to be competitive with existing seismometers deployed for science missions [14], the first step would be to demonstrate similar short-term sensitivity, which is around a few $\mathrm{nm/s^2/\sqrt{Hz}}$ (i.e., sub-μGal/$\sqrt{\mathrm{Hz}}$).

Atom interferometry has been a well-established technique for high-precision gravity measurement in the laboratory [15]. For mobile gravimeters, the sensitivity that has been achieved among the high-performance ones is, for example, 96 $\mathrm{nm/s^2/\sqrt{Hz}}$ in reference [16], or 500 $\mathrm{nm/s^2/\sqrt{Hz}}$ from commercially available gravimeters [17]. We note that several groups worldwide are developing mobile gravimeters, and reference [18] provides a comprehensive review. To reach a few $\mathrm{nm/s^2/\sqrt{Hz}}$, it is technically feasible with Bose–Einstein Condensate [19], matter-wave lensing [20], or large momentum transfers [21]; however, those techniques are not considered in the present version of ALS due to the typical size, weight, and power (SWaP) constraints for a lunar instrument, e.g., maximum mass of 35 kg and maximum keep-alive power consumption of 20 W for instruments that need to survive lunar nights in a lander [22].

Our motivation is to develop a compact instrument capable of operating within strict lunar SWaP constraints (e.g., 35 kg and 20 W, as mentioned above) while approaching quantum projection noise (QPN) limited sensitivity. Our strategy is taking advantage of lower lunar gravity for longer interferometer time and utilizing a simplified laser-cooled thermal atom source to achieve high sensitivity in a compact instrument. The ALS instrument sensor head is based on a 5 cm tall atomic fountain to reduce its dimensions and thus its mass.

In this work, we evaluate the feasibility of approaching the QPN-limited sensitivity using a standard Raman $\pi/2 - \pi - \pi/2$ pulse sequence. In this case, the QPN-limited sensitivity of the atom interferometer is

$$\Delta a = 1/(C \times \sqrt{N} \times k_{\mathrm{eff}} T^2), \tag{1}$$

where C is the fringe contrast, N is the atom number, and T is the interferometer time between the Raman laser pulses, and $k_{\mathrm{eff}} = 2(2\pi/\lambda) = 1.61 \times 10^7$ rad/m is the effective wavenumber of the two-photon Raman transition for rubidium atoms and $\lambda = 780$ nm for rubidium. The QPN-limited sensitivity in the 5 cm tall atomic fountain is summarized in Table 1.

Table 1. QPN-limited sensitivities of a Raman $\pi/2 - \pi - \pi/2$ atom interferometer, assuming contrast $C = 0.5$, $N = 10^6$ atoms, and 1 Hz data rate. The maximum time T between Raman laser pulses is $\sqrt{2h/g}$, where $h = 5$ cm and g is the surface gravity at the destination

Destination	Maximum Interferometer Time $2T$ [ms]	Sensitivity [$\mathrm{nm/s^2/\sqrt{Hz}}$]
Lunar surface	497	2
Earth surface	200	12

We measured a sensitivity of 1400 $\mathrm{nm/s^2/\sqrt{Hz}}$ with $T = 75$ ms, primarily limited by vibration noise in our lab. While our result shows a discrepancy of about two orders of magnitude relative to the QPN-limited sensitivity target with $T = 100$ ms on Earth, it provides a critical baseline for evaluating instrument performance under non-ideal conditions. To provide further context, we summarized the sensor head design and instrument implementation in Section 2. We then presented a comprehensive analysis of test results and current limitations in Section 3. Finally, future directions for improving the instrument are discussed in Section 4.

2. Materials and Methods

Compared to other mobile atom interferometers employing free-falling cold-atom samples or meter-scale atomic fountains with dedicated magnetic shields, our design utilizes a compact atomic fountain, thereby minimizing sensor head dimensions and total mass. The design strategy with a compact atomic fountain is specifically intended to bring the instrument within the strict SWaP constraints required for lunar deployment, where existing mobile atom interferometers remain logistically unfeasible. Despite a fountain height of just 5 cm, the system allows interferometer times up to $2T = 200$ ms on Earth. For an identical $2T$, a free-falling cold-atom sample would require a 20 cm drop; thus, the compact fountain reduces vertical dimension by a factor of four.

The fountain configuration has other added benefits, including allowing in situ variation in interrogation time for calibration, diagnosis, and other experiments, as well as the sensor head overall architecture suitable for operation in microgravity environment with and without launch requirements.

This work aims to reduce the mass of the sensor head. The laser system and control electronics were assembled using commercial-off-the-shelf components for laboratory measurements. Developing a flight model of the laser system and control electronics with significant SWaP reduction is possible but outside the scope of this study [23,24].

2.1. Sensor Head

The sensor head is based on an atomic fountain within an octagonal vacuum chamber maintained at 133×10^{-9} Pa (Figure 1). A rubidium-87 magneto-optical trap (MOT) at the center of the octagonal chamber loads atoms from background vapor. The atoms are launched upward and sub-Doppler cooled using moving molasses. In Earth gravity, the atoms are launched with an initial speed of 1 m/s so that the fountain's apex is 5 cm above the trap center. The round-trip flight time for the atoms to fall into the trap region is 200 ms. In lunar gravity, the atoms would be launched with an initial speed of 0.4 m/s so that round-trip flight would be about 0.5 s.

The octagonal vacuum chamber has an envelope dimension of 12×12 cm^2 and a thickness of 5 cm. The chamber is made of titanium with z-cut, anti-reflective-coated sapphire windows brazed to adapter rings and then welded to the chamber body. Compared to off-the-shelf stainless-steel chambers assembled with glass viewports, our octagonal vacuum chamber construction is lighter in weight and non-magnetic. The choice of sapphire window to minimize helium permeation opens the possibility of operating the vacuum chamber without an active ion pump [25–27]. However, this has not been tested and validated in this study.

The MOT, molasses, and detection laser beams use the same laser beam paths (hereafter referred to as the MOT beams), which include four 45-degree single-pass beams and one retro-reflected horizontal beam. Their e^{-2} beam diameter in intensity is 18 mm, large enough to prevent atoms from diffusing out from the MOT beam intersection during moving molasses stage when the launch speed is 1 m/s or lower. The state preparation and Raman laser take the vertical beam path (hereafter referred to as the Raman beam), and the beam diameter is 30 mm. One of the chamber's windows is recessed (Figure 1b). A Fresnel lens is inserted inside the recess to enhance photon collection efficiency onto a photodetector.

The MOT magnetic coils are centered about the horizontal MOT beam and are attached to the slightly recessed octagonal faces of the vacuum chamber. The inner spacing between the coils is 42 mm. There are three sets of rectangle coils for controlling the bias magnetic field. During state-preparation and interferometer, a quantization magnetic field of about 100 mG is applied in the vertical direction.

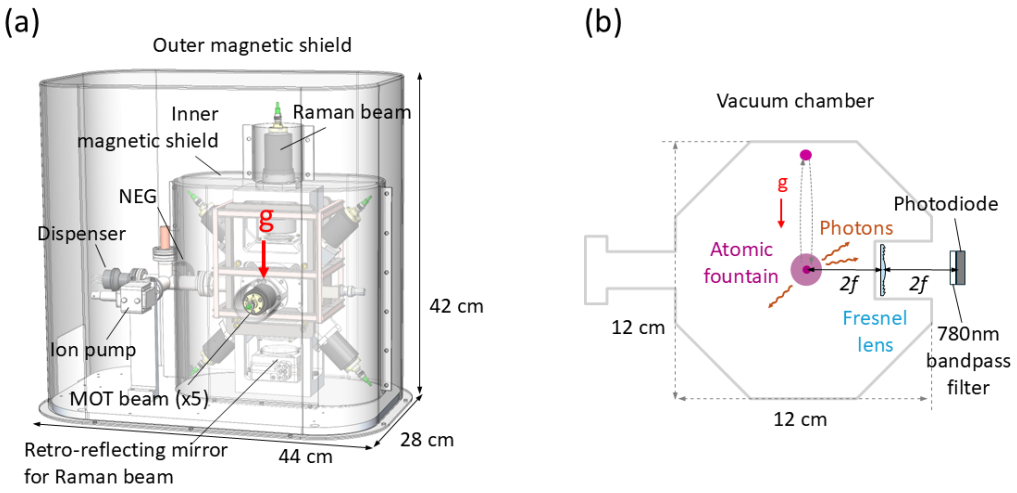


Figure 1. (**a**) The drawing of the sensor head. The enclosed volume of the outer magnetic shield is 52 L and the mass is 24 kg. The magnetic shields contribute to 70% of the mass. Elements in the space between the outer and inner magnetic shield include the 5-way cross hosting Rb dispensers, a non-evaporable getter (NEG) pump, an ion pump, and a copper tube for pinch-off sealing the vacuum. All optical components and magnetic coil packages are attached to an octagonal vacuum chamber, which is inside the inner magnetic shield. (**b**) Schematic of the atomic fountain inside the octagonal vacuum chamber.

Minimizing the magnetic field gradient is critical for longer interferometer times, as the fringe contrast can degrade due to the spatial variation in the quadratic Zeeman effect. We address this requirement as follows. The magnetic field gradient due to the rectangle coils within the region traversed by the atomic fountain is designed to be less than 2 mG/cm in all three directions (via finite element analysis) so that the fringe contrast reduction will be lower than 1% due to field inhomogeneity. The vacuum chamber, optics, and both sets of magnetic coils are enclosed within the inner magnetic shield, which blocks stray magnetic fields from the ion pump magnets. The ion pump is 20 cm away from the octagonal chamber center and the inner magnetic shield provides about 25 dB magnetic field attenuation. The inner and outer magnetic shields together provide more than 42 dB attenuation. The attenuation factors are estimated via finite element analysis and in that simulation the model of the shields is emersed in an uniform external magnetic field with a magnitude of 5 Gauss. The outer magnetic shield may not be necessary for the instrument operation on the surface of the Moon (or Mars) where the surface magnetic field is negligible compared to Earth magnetic field, which could potentially reduce the mass of the sensor head from 24 kg to 13 kg.

2.2. Laser System and Control Electronics

The laser system consists of two lasers (Figure 2). The first laser is a low-power 780 nm diode laser (linewidth 100 kHz), which is continuously locked to a ^{85}Rb transition line in a saturated absorption spectroscopy. The second laser is a frequency-doubled telecommunication laser system (the telecom laser) with output at 780 nm (linewidth 150 kHz). The telecom laser is locked to the diode laser with an offset frequency. Also, the 1560 nm seed of the telecom laser is phase modulated via a fiber-coupled electro-optical modulator (EOM). By switching the offset frequency and the modulation frequency, the carrier and the first-order sideband from the telecom laser address the ^{87}Rb transition frequencies required by the atom interferometer. It should be noted that with this EOM phase modulation scheme, the spurious sidebands from the EOM will limit the atom

interferometer accuracy to tens of 10 nm/s^2 [28], which is acceptable in this work but should be improved for lunar instruments.

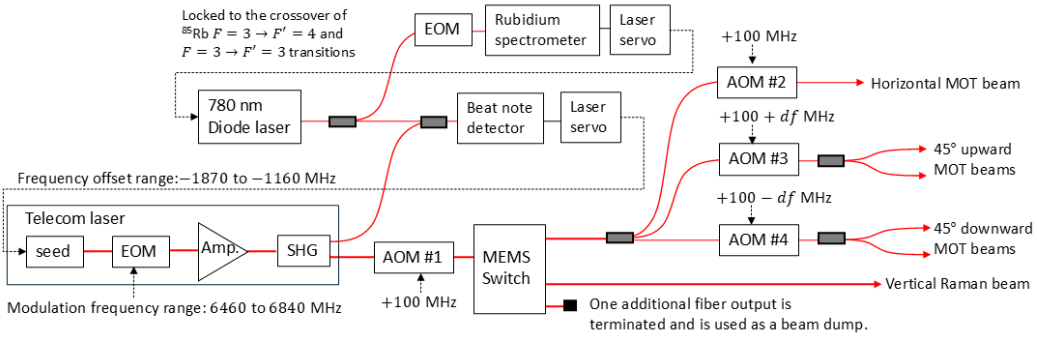


Figure 2. Schematic of the laser system.

The telecom laser's output level and pulse duration are controlled by a fiber-coupled acousto-optic modulator (AOM) operating at +100 MHz. The interferometer pulses of a few microseconds are generated using the fast-switching time of this AOM. The laser light is directed between the MOT and Raman beam paths with a micro-electromechanical system (MEMS) fiber switch. The laser light can be directed to an unused fiber output of the fiber switch to provide additional light extinction during the dark time between Raman laser pulses. The MOT beams pass additional fiber-coupled AOMs, allowing the detunings of the 45-degree beams to be controlled independently. The laser polarization is aligned to the slow axis of the fibers, and the AOM and MEMS components have a polarization–extinction ratio specification of 20 dB.

The modulation frequency and the offset frequency of the telecom laser are generated from two direct-digital synthesizers (DDSs) (by means of frequency up-conversion and frequency division, respectively). The DDSs are clocked by a hydrogen maser. The experimental control is based on a digital pattern generator, whose outputs trigger the DDSs and other components used to generate laser pulses, switch the magnetic field set points, and log the atom interferometer data. The pattern generator is also clocked by the same hydrogen maser source.

2.3. Atom Interferometer Operation Sequence

A typical atom interferometer measurement cycle starts with loading atoms into the MOT, followed by a three-step molasses cooling: pre-launch red molasses cooling, launch with moving molasses, and then post-launch cooling in (moving) Λ-enhanced grey molasses [29]. To implement the moving molasses, we change the detuning of the 45-degree beams relative to the horizontal beam. For initial velocity of $+1$ m/s, the two downward 45-degree beams are shifted by -0.9 MHz while the two upward 45-degree beam are shifted by $+0.9$ MHz (i.e., $df = \pm\frac{v_0}{\sqrt{2}\lambda}$ for the 45-degree beams). The differential detuning is within the bandwidth of the AOMs, which is about 10 MHz. The three-step molasses cooling takes about 7 ms to complete, and the final temperature of the atomic sample is below 3 μK.

The Raman beam is linear polarized and retro-reflected to create a linear–perpendicular–linear polarization configuration. To optically pump atoms to the initial state for atom interferometer operation, i.e., the $F = 1, m = 0$ state, the telecom laser's offset frequency and modulation frequency are tuned such that the carrier addresses the $F = 2 \rightarrow F' = 2$ transition while the first-order sideband addresses the $F = 1 \rightarrow F' = 0$ transition of ^{87}Rb. Because the quantization magnetic field is aligned with the Raman beam, and the polarization of the retro-reflected Raman beams is linear–perpendicular–linear, the first-

order sidebands effectively contain both σ^+ and σ^- components and not π component. The first-order sideband drives the $F = 1 \rightarrow F' = 0$ transition with $\Delta m = \pm 1$, leading to population in the $F = 1, m = 0$ state. During the interferometer with a $\pi/2 - \pi - \pi/2$ pulse sequence, the telecom laser's offset frequency is tuned so that the Raman single-photon detuning is -200 MHz from the $F = 2 \rightarrow F' = 0$ transition. This detuning is limited by the frequency tuning range of the telecom laser. The modulation frequency is at 6.834 GHz (the rubidium-87 hyperfine splitting frequency) plus a few MHz to compensate for the Doppler shift in the atomic fountain. The laser intensity at the center of the Raman beam is about 42 mW/cm^2 and the Raman π-pulse time is 5 µs. The pulse time is obtained experimentally from the Raman pulse Rabi oscillation curve.

The modulation power is adjusted to minimize the AC Stark shift in the two-photon Raman transition. Because the EOM is strongly driven, higher-order sidebands become significant and contribute to the overall AC Stark shift. We tune the microwave power applied to the EOM until the difference between the Raman transition frequency and the Doppler shift is less than 10 kHz for all three Raman pulses when using a 5 µs pulse duration. However, since this EOM phase modulation is applied at the seed-laser stage (before the internal power amplifier and second-harmonic generation of the telecom laser) the optimal microwave power must be re-adjusted whenever the laser operating conditions change.

After the interferometer, the final state of the atoms is detected when the atom cloud returns to the trap center. We use the MOT beams and apply a sequence of five pulses to measure the fraction of atoms transferred to the $F = 2$ state and plot the interferometer data as population ratio in the $F = 2$ state. The first pulse detects the atoms in the $F = 2$ state. The second pulse pumps the atoms in the $F = 1$ state to the $F = 2$ state so that the third pulse detects the total atom number. The forth pulse pumps atoms to the $F = 1$ state. The fifth pulse is applied after a delay of 4 ms so that it registers the reading due to laser light scattering and fluorescence due to background rubidium vapor. The duration of the pulses are: 170, 50, 170, 50, and 170 µs. There is typically a minimum of one million cold atoms at detection.

The frequency difference between the two Raman laser frequency components should be tuned at a rate of about $\alpha = 25.1$ kHz/ms to compensate for the Doppler shift due to Earth gravity. The Doppler shift changes sign depending on whether the atomic sample is in the ascending or descending phase of the fountain trajectory. In our case, the frequency difference is set by the modulation frequency, which is changed between the Raman laser pulses in discrete steps with a step size equals $\alpha \times T$. The DDS that controls the modulation frequency switches its output frequency between the first and the second Raman laser pulses, and then again between the second and the third Raman laser pulses; the time spacing between the actions is $T + 2\tau_R$, with $\tau_R = 2.5$ µs the $\pi/2-$pulse duration [15]. To scan the interferometer fringe, we introduce a phase by changing the DDS output frequency with a resolution around 1 Hz, i.e., effectively, scanning the chirp rate of the Raman lasers.

3. Results

A cloud of cold atoms will expand isotropically due to its finite temperature. With the same sensor head, the atom interferometer fringe contrast is expected to be lower for longer T, due to technical factors such as the expanded cold-atom cloud samples exhibiting more spatial inhomogeneity in the Raman beam profile. The instrument is tested in Earth gravity so that the maximum T is lower than that available in lunar gravity. To project the performance of our instrument on the lunar surface, we measure the fringe contrast as a function of T and extrapolate the data to estimate the contrast for longer T.

Figure 3a shows fringe contrast versus T from 10 ms to 90 ms. The fringe contrast is the amplitude of the sinusoidal fit of the fringe. The inset of Figure 3a shows an example of the fringe at $T = 75$ ms. Excluding the last point at $T = 90$ ms, we use a linear trend line to model the degradation of the fringe contrast, and the trend is $C = 0.67 - 0.0027T$ with T in units of ms.

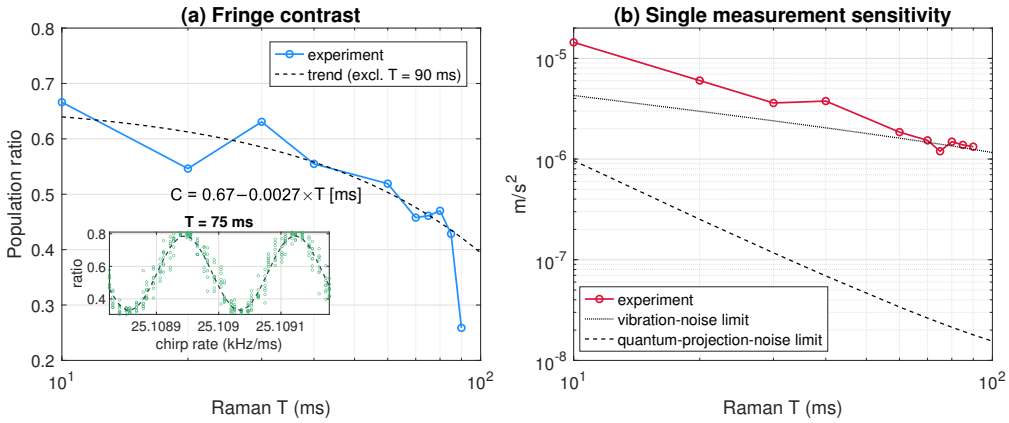


Figure 3. (**a**) Atom interferometer fringe contrast, measured for T from 10 ms to 90 ms. The dashed line is a linear trend of the degradation of the fringe contrast as a function of T. The line excludes the contribution from the last point at $T = 90$ ms. The inset shows an example of the atom interferometer fringe via scanning the Raman laser chirp rate. For each T, there are 328 points and the contrast C is the amplitude of the sinusoidal fit. (**b**) The sensitivity is estimated from how much the measurements scatter around the sinusoidal fit line; i.e., by dividing the root-mean-squared residual with $Ck_{\text{eff}}T^2$. The dotted line is the single-shot measurement noise due to the vibration in our lab. The dashed line is the QPN-limited sensitivity based on the fringe contrast in (**a**).

At $T = 90$ ms, the contrast is significantly lower because the mirror pulse is applied to the atoms near the apex of the atomic fountain, where the velocity of atoms is not sufficient to generate enough Doppler shift to distinguish the Doppler-sensitive Raman transitions from the Doppler-insensitive Raman transitions. With the present experimental parameters, a minimum speed of the cold-atom cloud of 10 cm/s is required to break the degeneracy. As a result, although the round-trip flight time of the atomic fountain in Earth gravity is 200 ms, to avoid the apex, the usable T is 90 ms. The available time can be extended by using longer Raman pulses (so that the transition linewidth is narrower) and applying a velocity selection pulse . A detailed explanation of this Raman degeneracy problem at near-zero velocity and the solutions have been investigated and can be found, e.g., in the works [30–32] and references therein.

We calculate the single-measurement sensitivity from the residuals of the sinusoidal fit and the sensitivity is plotted as a function of T in Figure 3b. The dotted line in Figure 3b is the atom interferometer's response to vibration noise per single measurement, calculated with the transfer function formalism in [33]. The vibration noise level of the vibration isolation platform on which the instrument is situated is around 3×10^{-7} m/s^2/$\sqrt{\text{Hz}}$ (see Figure 4b). As a result, for $T > 70$ ms in the sensitivity plot, the measured sensitivity is not the intrinsic noise of the instrument, but, rather, the signal due to the vibration.

In Figure 3b, the dashed line represents the QPN-limited sensitivity, which can be compared to the measured sensitivity to estimate the potential performance if vibration noise were absent. In this calculation, we assume $N = 10^6$, and the contrast C is taken from the contrast trend line in Figure 3a. According to the dashed line, it is projected to achieve 24 nm/s^2 per shot with $T = 75$ ms using our sensor head on the Earth's surface; however, measurements need to be performed at a vibrationally quiet site.

Figure 4 shows the Allan deviation and power spectral density of the atom interferometer acceleration measurement. The atom interferometer's output in population ratio (P) is logged as a time trace at a rate of 2.3 Hz and then converted to acceleration readings as $a = \frac{P}{C}\frac{1}{k_{\text{eff}}T^2}$. This data set contains 16,560 shots and with a data rate of 2.3 Hz, this translates into the lower limit in the power spectral density of 1.4×10^{-4} Hz. The contrast C is 0.45 and T is 75 ms. We choose $T = 75$ ms and not a longer T, so that even in the presence of vibration, the atom interferometer's output remains in the linear portion of the fringe and that the simple relation to convert the population ratio to acceleration is valid.

Based on the fitted line in Figure 4a, the instrument's short-term sensitivity is 1.4×10^{-6} m/s$^2/\sqrt{\text{Hz}}$ (140 μGal/$\sqrt{\text{Hz}}$), limited by the vibration noise in our lab, and it averages down to 6.7×10^{-8} m/s^2 (6.7 μGal) after 445 s. The frequency response of the instrument remains flat at frequencies down to 1 mHz. In contrast, classical sensors tend to have large drift at low frequency and long time scales. In the power spectral density plot, between 0.1 and 1 Hz, the noise level measured by the commercial seismometer agrees with the atom-interferometer signal, further indicating that the instrument sensitivity is vibration-limited.

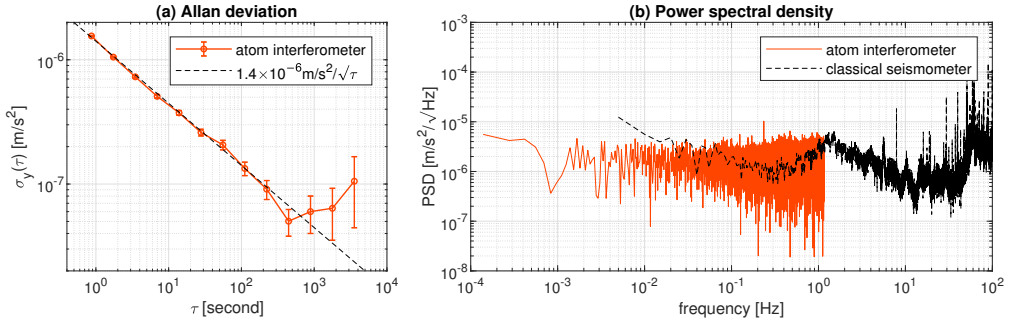


Figure 4. Acceleration measurement sensitivity and frequency response. Raman $T = 75$ ms. (**a**) Allan deviation, which averages down to 6.7×10^{-8} m/s^2 at 445 s. The dashed fitted line includes the data points up to $\tau = 445$ s. (**b**) Power spectral density, which remains flat down to 1 mHz (orange trace). The black dashed line is the vibration noise spectrum at our lab, measured with a commercial seismometer. Between 0.1 to 1 Hz, the noise level measured by the commercial seismometer agrees with the atom interferometer signal.

In contrast to alternative seismometer techniques that only sense ground motion, the atom interferometer can also measure absolute gravity. Figure 5 demonstrates this capability. A few fringe scans with different T are plotted on the same chart. The fringes have different fringe intervals, but they cross at the same chirp rate, where this chirp rate exactly cancels the Doppler shift due to the free fall of atoms in gravity. The value of gravity, g, is calculated using the equation $g = 2\pi \times \alpha_0/k_{\text{eff}}$, where α_0 is the chirp rate (in Hz/s) at which all the fringes intersect.

In the data set, each fringe is fitted with a sinusoidal function with T_i as a fixed parameter, while the fringe offset, fringe contrast, and initial phase (ϕ_i) are the free parameters, for fringe scan $i = 1, 2, 3$, etc. At the intersection of the fringes, $\Delta\Phi_L - 2\pi T_i \alpha = \phi_i$, where $\Delta\Phi_L$ is the phase due to the Raman lasers. We use the least-squares solution of the chirp rate α as our estimate of α_0.

The fringe intersection measurement is repeated for a few different non-zero magnetic field set points, as shown in Figure 5b. A minimal quantization magnetic field is required to break the degeneracy between the Zeeman m states. The data points are fitted with a second-order polynomial, and with zero magnetic field, the gravity value is estimated to be 9.795552 m/s^2. At our lab location, the surface gravity value interpolated from the U.S. National Geodetic Survey data is 9.79532 ± 0.00004 m/s^2 [34]. The measured value

agrees reasonably with the data. We note that several additional factors contribute to the systematic error in absolute gravity measurements, such as rubidium vapor pressure, Raman laser beam alignment, and Raman laser wavefront distortion [35], etc., and must be investigated in ultrahigh-precision gravity measurements. Further details can be found, e.g., in references [15,36–40].

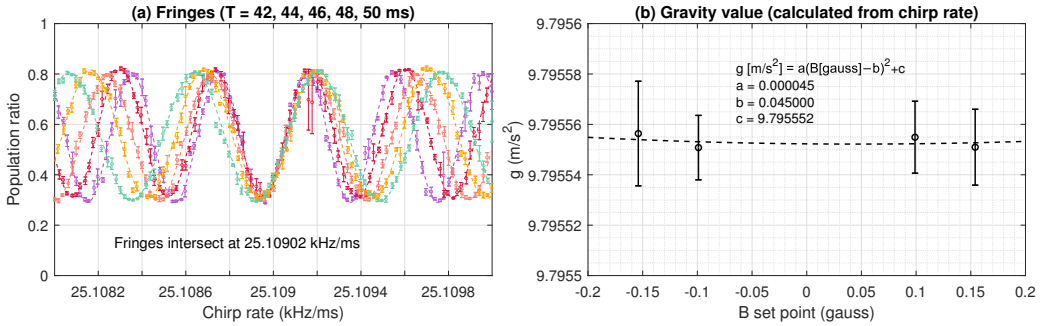


Figure 5. Gravity value measurement. (**a**) Atom interferometer fringes with different T. The fringes intersect at the Raman laser chirp rate that compensates for the Doppler shift due to the free falling in Earth gravity. (**b**) The measurement is repeated for a few magnetic field set points. Each data point is the average of the measurements with normal and reversed effective Raman wavevector (i.e., $+\vec{k}_{\text{eff}}$ and $-\vec{k}_{\text{eff}}$).

In Figure 4, we convert the time trace of population to acceleration using a simple relation. This approach assumes that fringe offset and contrast stay constant over long periods, which is unrealistic in our case. For example, we do not actively stabilize rubidium vapor pressure in the octagonal chamber or laser power in the beam paths. Environmental factors such as temperature and humidity in the lab are also unregulated.

To log the gravity value over a longer time scale, we use the phase quadrature method [41]. The method takes a set of four measurements, but in each subsequent measurement, the interferometer phase is increased by $\pi/2$ by stepping the Raman laser chirp rate. The four measurements are as follows.

$$P_1 = \frac{1}{2}[A - C\cos(\phi)] \quad (2)$$

$$P_2 = \frac{1}{2}[A - C\cos(\phi + \frac{\pi}{2})] \quad (3)$$

$$P_3 = \frac{1}{2}[A - C\cos(\phi + \pi)] \quad (4)$$

$$P_4 = \frac{1}{2}[A - C\cos(\phi + \frac{3}{2}\pi)] \quad (5)$$

The interferometer phase ϕ is calculated as follows.

$$\phi = \tan^{-1}\left(\frac{P_2 - P_4}{P_3 - P_1}\right) \quad (6)$$

Although the method returns one phase reading from four measurements (and reduces the measurement bandwidth), the fringe contrast C and fringe offset A both cancel out in the calculation. We use the method to measure the variation in the gravity value in our lab. As shown in Figure 6, there are modulations with amplitude around 200 μGal, which agrees reasonably with the solid Earth tide [42] calculated for our lab location.

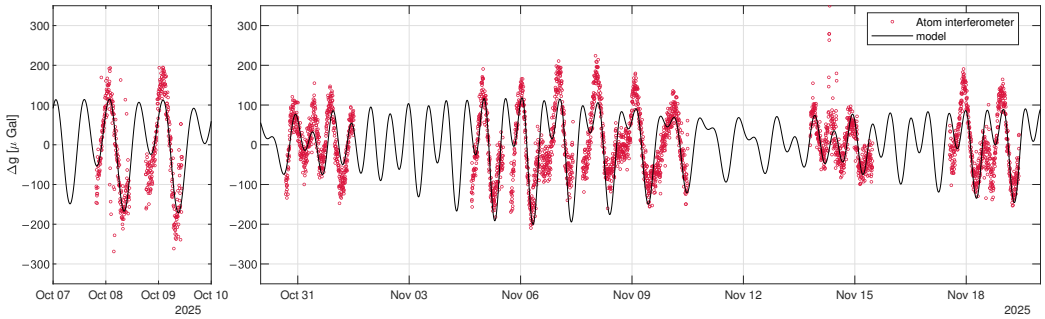


Figure 6. Modulation of the gravity value in our lab, measured with the phase quadrature method. Each data point is an average of 270 s of measurement. Raman $T = 75$ ms.

4. Discussion

Presently, our instrument's short-term sensitivity is 1400 $\mathrm{nm/s^2/\sqrt{Hz}}$ with $T = 75$ ms, limited by the vibration noise in our lab. Using the fringe contrast measured in Figure 3 to estimate the QPN-limited noise, it is feasible to reach 24 $\mathrm{nm/s^2/\sqrt{Hz}}$ with $T = 75$ ms when technical noises are suppressed.

In our sensor head, we did not include active vibration noise cancellation components, and this strategy stems from two main considerations. First, active cancellation may not be needed in a lunar environment if the instrument sensitivity is a few $\mathrm{nm/s^2/\sqrt{Hz}}$. Apollo data show that lunar seismic noise in the vertical direction is as low as 10^{-10} $\mathrm{m/s^2/\sqrt{Hz}}$ at 0.1 to 1 Hz [14], which is not detectable at current sensitivity levels. Second, because of typical SWaP constraints for lunar instruments, we want to explore if it is possible to reach QPN-limited sensitivity without adding components beyond those directly supporting the basic $\pi/2 - \pi - \pi/2$ Raman interferometer operation. For similar considerations, we did not include Coriolis compensation components in our sensor head because Moon's rotation rate is about 27 times slower than Earth.

We acknowledge that the QPN limit extrapolation alone is insufficient to validate the instrument's performance. Experimental demonstration is needed to show a sensitivity of about 12 $\mathrm{nm/s^2/\sqrt{Hz}}$ on Earth's surface, as summarized in Table 1. Our follow-up plan is to build a transportable laser system and control electronics. We will then repeat the same measurement in a seismic vault, which provides lower background seismic noise. For example, the seismic vault on the Jet Propulsion Laboratory campus is appropriate for validation.

In addition to repeating the measurement in a seismic vault, improvements toward reaching the QPN-limited sensitivity include reducing the molasses temperature (to minimize sampling of Raman beam inhomogeneities) and applying Raman velocity-selection pulses (to narrow the velocity distribution along the Raman beam direction). Certain design choices should be avoided in future iterations, such as operating without active regulation of laser power or rubidium vapor pressure.

The MOT is loaded from the background rubidium vapor in the octagon chamber, with a loading time of about 200 ms. The fountain configuration may aid in re-capturing atoms into the MOT, but the launch process can also introduce losses (e.g., atoms drifting sideways due to imperfect beam alignment or intensity imbalance in the 45-degree configuration). As a result, we cannot reduce the MOT loading time further while maintaining our target of operating at about one million atoms. The launch efficiency has not yet been characterized.

5. Conclusions

In this paper, we summarize our instrument design target for lunar applications and present test results from a laboratory environment. Our instrument uses Raman atom

interferometry and a 5 cm tall atomic fountain. Presently, the instrument's short-term sensitivity is 1.4×10^{-6} m/s^2/$\sqrt{\text{Hz}}$ with Raman $T = 75$ ms, limited by vibration noise in our lab. This uncertainty averages down to 6.7×10^{-8} m/s^2 after 445 s. To advance this instrument, the next step is to perform measurements in seismic vaults that have lower seismic noise.

Author Contributions: All authors contributed to the design and technical discussions presented here. N.Y. is the PI, directed and oversaw the technical implementation and development. Y.-J.C. built the prototype and conducted the measurements. The manuscript was written by Y.-J.C. and F.B., with revisions and edits from S.-w.C. and N.Y. All authors have read and agreed to the published version of the manuscript.

Funding: The research was carried out at the Jet Propulsion Laboratory, California Institute of Technology, under a contract with the National Aeronautics and Space Administration. ©2026. California Institute of Technology. Government sponsorship acknowledged.

Data Availability Statement: The original contributions presented in this study are included in the article. Further inquiries can be directed to the corresponding author.

Acknowledgments: We wish to express our appreciation for the contribution of Hector Mas in the early stage of our work. We are grateful for the valuable discussions with Saesun Kim and Tin Nguyen. We acknowledge the Frequency and Timing Advanced Instrument Development Group for their ever-present support with the hydrogen maser source.

Conflicts of Interest: The authors declare no conflicts of interest.

References

1. Lognonné, P. Planetary seismology. *Annu. Rev. Earth Planet. Sci.* **2005**, *33*, 571–604. [CrossRef]
2. Dziewonski, A.M.; Gilbert, F. Solidity of the Inner Core of the Earth inferred from Normal Mode Observations. *Nature* **1971**, *234*, 465–466. [CrossRef]
3. Park, J.; Song, T.R.A.; Tromp, J.; Okal, E.; Stein, S.; Roult, G.; Clevede, E.; Laske, G.; Kanamori, H.; Davis, P.; et al. Earth's Free Oscillations Excited by the 26 December 2004 Sumatra-Andaman Earthquake. *Science* **2005**, *308*, 1139–1144. [CrossRef] [PubMed]
4. Weber, R.C.; Lin, P.Y.; Garnero, E.J.; Williams, Q.; Lognonné, P. Seismic Detection of the Lunar Core. *Science* **2011**, *331*, 309–312. [CrossRef] [PubMed]
5. Nunn, C.; Garcia, R.F.; Nakamura, Y.; Marusiak, A.G.; Kawamura, T.; Sun, D.; Margerin, L.; Weber, R.; Drilleau, M.; Wieczorek, M.A.; et al. Lunar Seismology: A Data and Instrumentation Review. *Space Sci. Rev.* **2020**, *216*, 89. [CrossRef]
6. Zuber, M.T.; Smith, D.E.; Watkins, M.M.; Asmar, S.W.; Konopliv, A.S.; Lemoine, F.G.; Melosh, H.J.; Neumann, G.A.; Phillips, R.J.; Solomon, S.C.; et al. Gravity Field of the Moon from the Gravity Recovery and Interior Laboratory (GRAIL) Mission. *Science* **2013**, *339*, 668–671. [CrossRef] [PubMed]
7. Wieczorek, M.A.; Neumann, G.A.; Nimmo, F.; Kiefer, W.S.; Taylor, G.J.; Melosh, H.J.; Phillips, R.J.; Solomon, S.C.; Andrews-Hanna, J.C.; Asmar, S.W.; et al. The Crust of the Moon as Seen by GRAIL. *Science* **2013**, *339*, 671–675. [CrossRef] [PubMed]
8. Andrews-Hanna, J.C.; Asmar, S.W.; Head, J.W.; Kiefer, W.S.; Konopliv, A.S.; Lemoine, F.G.; Matsuyama, I.; Mazarico, E.; McGovern, P.J.; Melosh, H.J.; et al. Ancient Igneous Intrusions and Early Expansion of the Moon Revealed by GRAIL Gravity Gradiometry. *Science* **2013**, *339*, 675–678. [CrossRef] [PubMed]
9. Haviland, H.F.; Weber, R.C.; Neal, C.R.; Lognonné, P.; Garcia, R.F.; Schmerr, N.; Nagihara, S.; Grimm, R.; Currie, D.G.; Dell'Agnello, S.; et al. The lunar geophysical network landing sites science rationale. *Planet. Sci. J.* **2022**, *3*, 40. [CrossRef]
10. Panning, M.; Kedar, S.; Bowles, N.; Calcutt, S.; Drilleau, M.; Garcia, R.; Kawamura, T.; Lognonné, P.; Mimoun, D.; Nunn, C.; et al. Farside Seismic Suite (FSS): First-ever seismology on the farside of the Moon and a model for long-lived lunar science. In Proceedings of the Europlanet Science Congress 2022, Granada, Spain, 18–23 September 2022; EPSC2022-672. [CrossRef]
11. Lognonné, P.; Banerdt, W.B.; Giardini, D.; Pike, W.T.; Christensen, U.; Laudet, P.; De Raucourt, S.; Zweifel, P.; Calcutt, S.; Bierwirth, M.; et al. SEIS: Insight's seismic experiment for internal structure of Mars. *Space Sci. Rev.* **2019**, *215*, 12. [CrossRef] [PubMed]
12. van Heijningen, J.V.; ter Brake, H.J.M.; Gerberding, O.; Chalathadka Subrahmanya, S.; Harms, J.; Bian, X.; Gatti, A.; Zeoli, M.; Bertolini, A.; Collette, C.; et al. The payload of the Lunar Gravitational-wave Antenna. *J. Appl. Phys.* **2023**, *133*, 244501. [CrossRef]
13. Ajith, P.; Seoane, P.A.; Sedda, M.A.; Arcodia, R.; Badaracco, F.; Banerjee, B.; Belgacem, E.; Benetti, G.; Benetti, S.; Bobrick, A.; et al. The Lunar Gravitational-wave Antenna: Mission studies and science case. *J. Cosmol. Astropart. Phys.* **2025**, *2025*, 108. [CrossRef]

14. Lognonné, P.; Johnson, C. 10.03—Planetary Seismology. In *Treatise on Geophysics*, 2nd ed.; Schubert, G., Ed.; Elsevier: Oxford, UK, 2015; pp. 65–120. [CrossRef]
15. Peters, A.; Chung, K.Y.; Chu, S. High-precision gravity measurements using atom interferometry. *Metrologia* **2001**, *38*, 25. [CrossRef]
16. Freier, C.; Hauth, M.; Schkolnik, V.; Leykauf, B.; Schilling, M.; Wziontek, H.; Scherneck, H.G.; Müller, J.; Peters, A. Mobile quantum gravity sensor with unprecedented stability. *J. Phys. Conf. Ser.* **2016**, *723*, 012050. [CrossRef]
17. Quantum Gravimeters. Available online: https://www.exail.com/product/quantum-gravimeters (accessed on 16 May 2026) .
18. Fang, J.; Wang, W.; Zhou, Y.; Li, J.; Zhang, D.; Tang, B.; Zhong, J.; Hu, J.; Zhou, F.; Chen, X.; et al. Classical and Atomic Gravimetry. *Remote Sens.* **2024**, *16*, 2634. [CrossRef]
19. Abend, S.; Gebbe, M.; Gersemann, M.; Ahlers, H.; Müntinga, H.; Giese, E.; Gaaloul, N.; Schubert, C.; Lämmerzahl, C.; Ertmer, W.; et al. Atom-Chip Fountain Gravimeter. *Phys. Rev. Lett.* **2016**, *117*, 203003. [CrossRef] [PubMed]
20. Kovachy, T.; Hogan, J.M.; Sugarbaker, A.; Dickerson, S.M.; Donnelly, C.A.; Overstreet, C.; Kasevich, M.A. Matter Wave Lensing to Picokelvin Temperatures. *Phys. Rev. Lett.* **2015**, *114*, 143004. [CrossRef] [PubMed]
21. Chiow, S.w.; Kovachy, T.; Chien, H.C.; Kasevich, M.A. 102$\hbar k$ Large Area Atom Interferometers. *Phys. Rev. Lett.* **2011**, *107*, 130403. [CrossRef] [PubMed]
22. NASA Research Announcement: Payloads and Research Investigations on the Surface of the Moon. Available online: https://nspires.nasaprs.com/external/solicitations/summary.do?solId=%7b7D2A1FB4-62A6-7691-D879-8E06168F12EF%7d&path=&method=init (accessed on 16 May 2026).
23. Bagheri, M.; Hunacek, J.; Kittlaus, E.; Langlois, M.; Nejadriahi, H.; Yasar, F.; wey Chiow, S.; Yu, N.; Forouhar, S. All-semiconductor-based systems for atom interferometry experiments in space. *J. Opt. Soc. Am. B* **2024**, *41*, 1979–1986. [CrossRef]
24. Kittlaus, E.; Hunacek, J.; Bagheri, M.; Nejadriahi, H.; Langlois, M.; Chiow, S.w.; Yu, N.; Forouhar, S. Semiconductor optical amplifier-based laser system for cold-atom sensors. *EPJ Quantum Technol.* **2025**, *12*, 46. [CrossRef] [PubMed]
25. Boudot, R.; McGilligan, J.P.; Moore, K.R.; Maurice, V.; Martinez, G.D.; Hansen, A.; de Clercq, E.; Kitching, J. Enhanced observation time of magneto-optical traps using micro-machined non-evaporable getter pumps. *Sci. Rep.* **2020**, *10*, 16590. [CrossRef] [PubMed]
26. Little, B.J.; Hoth, G.W.; Christensen, J.; Walker, C.; De Smet, D.J.; Biedermann, G.W.; Lee, J.; Schwindt, P.D. A passively pumped vacuum package sustaining cold atoms for more than 200 days. *AVS Quantum Sci.* **2021**, *3*, 035001. [CrossRef]
27. Hoang, T.M.; Chung, S.K.; Le, T.; Park, S.; Park, S.J.; Eden, J.G.; Holland, C.; Wang, H.; Momeni, O.; Bradley, R.; et al. Micro mercury trapped ion clock prototypes with 10-14 frequency stability in 1-liter packages. *Sci. Rep.* **2023**, *13*, 10629. [CrossRef] [PubMed]
28. Carraz, O.; Charrière, R.; Cadoret, M.; Zahzam, N.; Bidel, Y.; Bresson, A. Phase shift in an atom interferometer induced by the additional laser lines of a Raman laser generated by modulation. *Phys. Rev. A* **2012**, *86*, 033605. [CrossRef]
29. Rosi, S.; Burchianti, A.; Conclave, S.; Naik, D.S.; Roati, G.; Fort, C.; Minardi, F. Λ-enhanced grey molasses on the D2 transition of Rubidium-87 atoms. *Sci. Rep.* **2018**, *8*, 1301. [CrossRef] [PubMed]
30. Lévèque, T.; Gauguet, A.; Michaud, F.; Pereira Dos Santos, F.; Landragin, A. Enhancing the Area of a Raman Atom Interferometer Using a Versatile Double-Diffraction Technique. *Phys. Rev. Lett.* **2009**, *103*, 080405. [CrossRef] [PubMed]
31. Perrin, I.; Bernard, J.; Bidel, Y.; Bonnin, A.; Zahzam, N.; Blanchard, C.; Bresson, A.; Cadoret, M. Zero-velocity atom interferometry using a retroreflected frequency-chirped laser. *Phys. Rev. A* **2019**, *100*, 053618. [CrossRef]
32. Bernard, J.; Bidel, Y.; Cadoret, M.; Salducci, C.; Zahzam, N.; Schwartz, S.; Bonnin, A.; Blanchard, C.; Bresson, A. Atom interferometry using $\sigma^+ - \sigma^-$ Raman transitions between $|F = 1, m_F = \mp 1\rangle$ and $|F = 2, m_F = \pm 1\rangle$. *Phys. Rev. A* **2022**, *105*, 033318. [CrossRef]
33. Cheinet, P.; Canuel, B.; Pereira Dos Santos, F.; Gauguet, A.; Yver-Leduc, F.; Landragin, A. Measurement of the Sensitivity Function in a Time-Domain Atomic Interferometer. *IEEE Trans. Instrum. Meas.* **2008**, *57*, 1141–1148. [CrossRef]
34. NGS Surface Gravity Prediction. Available online: https://www.ngs.noaa.gov/cgi-bin/grav_pdx.prl (accessed on 16 May 2026).
35. Junca, J.; Kitching, J.; McGehee, W. Wavefront Mapping for Absolute Atom Interferometry. *Phys. Rev. Lett.* **2026**, *136*, 143402. [CrossRef] [PubMed]
36. Hauth, M.; Freier, C.; Schkolnik, V.; Peters, A.; Wziontek, H.; Schilling, M. Atom interferometry for absolute measurements of local gravity. In *Atom Interferometry*; IOS Press: Amsterdam, The Netherlands, 2014; pp. 557–603.
37. Ménoret, V.; Vermeulen, P.; Le Moigne, N.; Bonvalot, S.; Bouyer, P.; Landragin, A.; Desruelle, B. Gravity measurements below 10^{-9} g with a transportable absolute quantum gravimeter. *Sci. Rep.* **2018**, *8*, 12300. [CrossRef] [PubMed]
38. Wu, X.; Pagel, Z.; Malek, B.S.; Nguyen, T.H.; Zi, F.; Scheirer, D.S.; Müller, H. Gravity surveys using a mobile atom interferometer. *Sci. Adv.* **2019**, *5*, eaax0800. [CrossRef] [PubMed]
39. Fu, Z.; Wu, B.; Cheng, B.; Zhou, Y.; Weng, K.; Zhu, D.; Wang, Z.; Lin, Q. A new type of compact gravimeter for long-term absolute gravity monitoring. *Metrologia* **2019**, *56*, 025001. [CrossRef]

40. Xu, Y.Y.; Cui, J.F.; Qi, K.; Chen, L.L.; Deng, X.B.; Luo, Q.; Zhang, H.; Tan, Y.J.; Shao, C.G.; Zhou, M.K.; et al. Evaluation of the transportable atom gravimeter HUST-QG. *Metrologia* **2022**, *59*, 055001. [CrossRef]
41. Chen, Y.J.; Hansen, A.; Shuker, M.; Boudot, R.; Kitching, J.; Donley, E.A. Robust inertial sensing with point-source atom interferometry for interferograms spanning a partial period. *Opt. Express* **2020**, *28*, 34516–34529. [CrossRef] [PubMed]
42. Wenzel, H.G. *Eterna–Programs for Tidal Analysis and Prediction*; Karlsruhe Institute of Technology: Karlsruhe, Germany, 2022. [CrossRef] [PubMed]

Disclaimer/Publisher's Note: The statements, opinions and data contained in all publications are solely those of the individual author(s) and contributor(s) and not of MDPI and/or the editor(s). MDPI and/or the editor(s) disclaim responsibility for any injury to people or property resulting from any ideas, methods, instructions or products referred to in the content.